Vertical Structure of Dissipation in the Nearshore — **Source link** ⬏

Falk Feddersen, John H. Trowbridge, Albert J. Williams

Institutions: Scripps Institution of Oceanography, Woods Hole Oceanographic Institution

Topics: Dissipation, Breaking wave, Boundary layer, Turbulence kinetic energy and Turbulence

Related papers:

- Observations of turbulence in the ocean surface boundary layer : energetics and transport

- Estimates of Kinetic Energy Dissipation under Breaking Waves

- The Influence of Whitecapping Waves on the Vertical Structure of Turbulence in a Shallow Estuarine Embayment

- Modeling Wave-Enhanced Turbulence in the Ocean Surface Layer

- Oceanic Turbulence Dissipation Measurements in SWADE

Vertical Structure of Dissipation in the Nearshore

FALK FEDDERSEN

Scripps Institution of Oceanography, La Jolla, California

J. H. TROWBRIDGE AND A. J. WILLIAMS III

Woods Hole Oceanographic Institution, Woods Hole, Massachusetts

ABSTRACT

The vertical structure of the dissipation of turbulence kinetic energy was observed in the nearshore region (3.2-m mean water depth) with a tripod of three acoustic Doppler current meters off a sandy ocean beach. Surface and bottom boundary layer dissipation scaling concepts overlap in this region. No depth-limited wave breaking occurred at the tripod, but wind-induced whitecapping wave breaking did occur. Dissipation is maximum near the surface and minimum at middepth, with a secondary maximum near the bed. The observed dissipation does not follow a surfzone scaling, nor does it follow a "log layer" surface or bottom boundary layer scaling. At the upper two current meters, dissipation follows a modified deep-water breaking-wave scaling. Vertical shear in the mean currents is negligible and shear production magnitude is much less than dissipation, implying that the vertical diffusion of turbulence is important. The increased near-bed secondary dissipation maximum results from a decrease in the turbulent length scale.

1. Introduction

Turbulence plays a key role in vertical mixing of momentum, sediment, buoyancy, and other tracers in the ocean. Oceanic turbulence is often studied by examining the rate of turbulent kinetic energy dissipation ε. In deep water, near-surface turbulence is often elevated above that expected for a free-surface log layer (Csanady 1984) because of whitecapping breaking of surface gravity waves (Agrawal et al. 1992; Anis and Moum 1995; Terray et al. 1996; Drennan et al. 1996) associated with strong winds. Terray et al. (1996) showed that near-surface dissipation scales as $\varepsilon \sim (z'/H_{\text{sig}})^{-2}$, where z' is the distance from the surface and H_{sig} is the significant wave height, and not as $\varepsilon \sim z'^{-1}$, as would be expected for a free-surface log layer (Csanady 1984) with a balance between shear production and dissipation. The ε magnitude scales with energy lost because of wave breaking, demonstrating that elevated near-surface dissipation is linked to wave breaking. The departure from log-layer scaling implies that the turbulence

dynamics are not shear production balancing dissipation, but that other terms such as vertical diffusion of turbulence are important. Two equation turbulence models (e.g., Mellor and Yamada 1982; Rodi 1987) can (with modifications) reproduce the deep-water near-surface ε scalings (Craig and Banner 1994; Terray et al. 1999; Burchard 2001; Umlauf and Burchard 2003) and predict enhanced ε relative to shear production. Recently, additional near-surface ε data obtained using microstructure profilers from the tropical Pacific (Soloviev and Lukas 2003) and a Swiss lake (Stips et al. 2005) have confirmed the Terray et al. (1996) ε scaling.

Near the seabed, in the bottom boundary layer (BBL), turbulence is generated by vertical shear of the mean flow. In the absence of stratification, this results in a classic "log layer" where the velocity profile is logarithmic and the dissipation scales as

$$\varepsilon = \frac{u_*^3}{\kappa z}, \tag{1}$$

where u_* is the bed friction velocity (i.e., ρu_*^2 is the bottom stress), κ is the empirical von Kármán's constant, and z is the height above the bed (with bed roughness incorporated or assuming $z_0 \ll z$). Grant and Madsen (1979) generalized the Prandtl–Karman law of

Corresponding author address: F. Feddersen, SIO, 9500 Gilman Dr., La Jolla, CA 92093-0209.
E-mail: falk@coast.ucsd.edu

the wall or log layer to the continental shelf bottom boundary layer (BL) in the presence of wave-orbital velocities and bottom roughness.

In a tidal boundary layer without surface gravity waves, Gross and Nowell (1985) found that the BBL ε scaling (1) applied over the bottommost 4 m and that shear production (inferred from logarithmic velocity profiles) balanced ε. Similarly, from microstructure measurements within a few meters of the bed, $\varepsilon \sim z^{-1}$ on the continental shelf (Dewey and Crawford 1988) and in the Hudson River estuary (Peters and Bokhorst 2000), suggesting that (1) largely applied. In the Hudson River estuary BBL without surface gravity waves, shear production estimated from directly measured Reynolds stresses balanced ε (Trowbridge et al. 1999). Shear production also balanced ε on the continental shelf BBL (60-m water depth) in the presence of energetic surface gravity waves (Shaw et al. 2001), with ε decreasing with height above the bed. Two-equation turbulence models usually work well in BBL regions (e.g., Mellor and Yamada 1982; Umlauf and Burchard 2003).

In the nearshore region with depths roughly <5 m, the surface and bottom boundary layer regions overlap, and the turbulence dynamics and scaling of ε are not understood. In the surfzone, strong depth-limited wave breaking (resulting in a shoreward-propagating self-similar bore) dominates turbulence in most of the water column. Surfzone ε measurements from different beaches and wave conditions (George et al. 1994; Bryan et al. 2003) are collapsed by a surfzone ε scaling (assuming constant wave height to water depth), which was reproduced by a surfzone modified k–ε model (Feddersen and Trowbridge 2005).

Offshore of the surfzone but still within the nearshore, strong winds lead to whitecapping-style wave breaking (which does not result in a self-similar bore) just as in the open ocean. In finite depth, the probability of such wave breaking is increased over deep-water conditions (Babanin et al. 2001). Bottom boundary layer processes are also important. In 4.5-m mean water depth, measurements at 1 m above the bed during active wave-breaking conditions ($H_{\mathrm{sig}} > 1.8$ m) showed a balance between shear production and ε [Trowbridge and Elgar 2001, hereinafter TE01], with no indication of enhanced ε as expected under breaking waves (e.g., Agrawal et al. 1992; Terray et al. 1996). However, the mean alongshore currents were strong (>1 m s^{-1}) during wave breaking. Feddersen and Trowbridge (2005) showed that these measurements likely were dominated by BBL dynamics and were too close to the bed to see breaking-wave-enhanced ε.

Here, nearshore dissipation observations from a vertical array of current meters in 3.2-m mean water depth are examined. At this location depth-limited wave breaking typical of the surfzone was not observed, but whitecapping-style wave breaking and microbreaking were observed. Observations are described in section 2. In this wave-dominated environment, dissipation ε is calculated from observed velocity power spectra and a kinematic model (Lumley and Terray 1983) for the wave advection of frozen turbulence (see section 3 and appendix). Several consistency checks are applied to make sure the estimates of ε are reasonable, and EOF decomposition is used to characterize the vertical structure of ε.

The ε observations are examined in sections 4 and 5. Closest to the surface ε is maximum, with a middepth minimum and a secondary maximum closer to the bed. As expected, the observed ε do not follow a surfzone scaling for ε. Bottom and surface boundary layer (SBL) scalings also underpredict the observed ε, indicating that logarithmic laws of the wall scaling do not apply. Indeed, shear production magnitude is much smaller than the ε. The deep-water wave-breaking ε scaling of Terray et al. (1996) applies at the two uppermost current meters. This indicates that the turbulence dynamics balance downward diffusion of turbulence against ε. The increased ε at the lowest current meter is consistent with the turbulence length scale decreasing near the bed, with the same turbulence dynamics.

2. Observations

As described in Feddersen and Williams (2007), the measurements were collected during September 2002 off a barrier island exposed to the Atlantic Ocean near Duck, North Carolina, at the U.S. Army Corps of Engineers Field Research Facility (FRF). The coordinate system (x, y, and z where $z = 0$ at the bed) is defined so that u, v, and w are the velocities in the offshore, alongshore, and upward direction. A vertical array of three Sontek Acoustic Doppler Velocimeters (ADV) was deployed on a tripod 140 m from shore in 3.2-m mean depth (Fig. 1) with ±0.4-m tide range. At this location the beach slope is 0.025, and offshore of the sandbar (90 m from shore) the bathymetry was highly alongshore uniform. The tripod orientation, pitch, and roll were determined by surveying the exposed tripod corners. The tripod tilt was consistent with the surveyed beach slope near the tripod. High-quality data were collected for 56 h starting at 1200 EST 22 September 2002.

The ADV has been both tested (Elgar et al. 2001) and used in turbulence studies (Trowbridge and Elgar 2001, 2003) in the nearshore and surfzone regions. The 3 ADVs (denoted ADV 1, 2, and 3) had sensing vol-
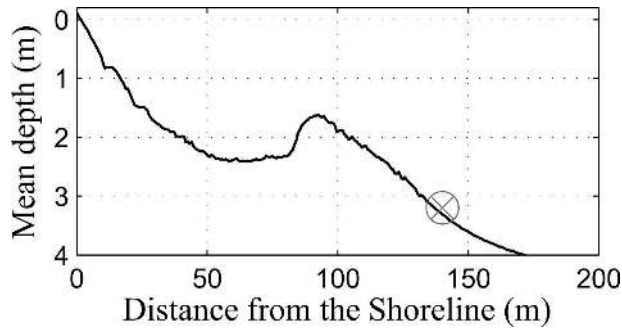
FIG. 1. Mean depth profile vs distance from the shoreline from a survey on 17 Sep 2002. The symbol marks the tripod location.

umes at heights of 0.56, 1.32, and 1.86 m above the bed, respectively (Fig. 2). ADVs 2 and 3 were stacked vertically and oriented sideways in the northward $(+y)$ alongshore direction. The bottommost ADV 1 had an upward-looking orientation, and its sensing volume was offset 0.56 m in the alongshore direction from ADVs 2 and 3 (Fig. 2). ADV velocities were measured at 12.5 Hz in hourly bursts of 24.8 min (18 572 data points). Data quality was high and is discussed in Feddersen and Williams (2007). The three components of ADV measured velocity were transformed (rotated) into cross-shore u (positive offshore), alongshore v (positive northward), and vertical w (positive upward) components and processed into burst means ($\bar{u}$, $\bar{v}$, $\bar{w}$) and standard deviations (σ_u, σ_v, σ_w). The mean cross-shore velocities $|\bar{u}| < 0.1$ m s^{-1} at all three ADVs, typically smaller than the alongshore current $\bar{v}$. The mean vertical velocities $\bar{w}$ at all three ADVs are weak ($|\bar{w}| < 0.01$ m s^{-1}), indicating that the coordinate transformation is reasonable. The significant wave height H_{sig} varied between 0.7 and 1.2 m (Fig. 3) and the peak period between 9 and 10 s, resulting in typical $kh = 0.41$ (k is the wavenumber). The orbital wave velocity standard deviation σ_u varied between 0.2 and 0.5 m s^{-1}, and σ_v was about one-half of σ_u. The vertical orbital velocities (σ_w) are also significant and increase with height above the bed consistent with linear theory [i.e., $\sigma_w \sim \sinh(kz) \sim kz$].

With northward alongshore current (positive $\bar{v}$), the instruments measure in the lee of the tripod mast, and significant mast-induced flow disturbance is evident [see discussion in Feddersen and Williams (2007)]. To minimize flow disturbance effects, the turbulence analysis is restricted to cases where the lowest instrument (ADV 1) has $\bar{v} < -0.16$ m s^{-1} (Fig. 3c). This cutoff is chosen as a trade-off between minimizing flow disturbance and having sufficient data points for the analysis. For the 56 h of data, 47 h satisfy this criteria, where on average $\bar{v} = -0.23$ m s^{-1} and $\sigma_u = 0.31$ m s^{-1}.

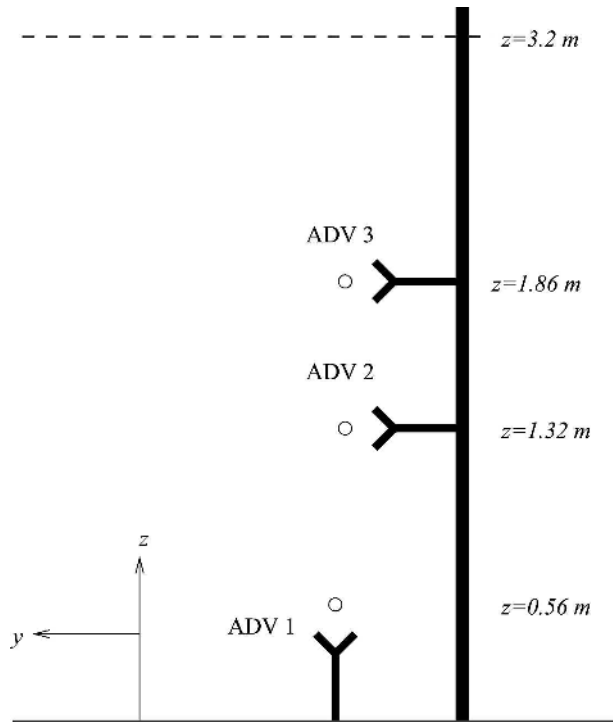Wind speed and direction measured 19.5 m above

FIG. 2. Schematic of the ADV locations. The view is toward offshore $(+x)$, and the vertical z and alongshore y coordinates are indicated. ADV 1 is upward looking. The vertical locations of the ADV sensing volumes (indicated by the small circle) are given. ADV 1 is offset 0.56 m alongshore from the sensing volumes of ADVs 2 and 3. The dashed horizontal line indicates the location of the mean sea surface at $z = 3.2$ m.

mean sea level at the end of the nearby FRF pier are used to estimate wind stress using the algorithm of Large and Pond (1981). No corrections were made for the possible significant effect of waves and whitecapping on the wind stress (e.g., Donelan 1990; Rieder et al. 1996; Drennan et al. 1999). The estimated alongshore wind stress τ_y^w/ρ is on the order of 10^{-4} m^2 s^{-2}. For the 47 good hours of data, the alongshore wind stress is related to a quadratic drag law for the bottom stress, that is,

$$\tau_y^w/\rho = c_d \overline{|\mathbf{u}|v}, \tag{2}$$

where c_d is a nondimensional drag coefficient and $\mathbf{u}$ is the horizontal velocity vector. The balance (2) is applied with ADV 1 velocity observations averaged over the 24.8-min burst. The skill of the balance (2) over the 56 h of data is high (correlation $r = 0.8$), indicating a wind-driven alongshore current. The best-fit c_d is consistent with the seaward of the surfzone momentum balances derived $c_d = 10^{-3}$ at the same beach (Feddersen et al. 1998).

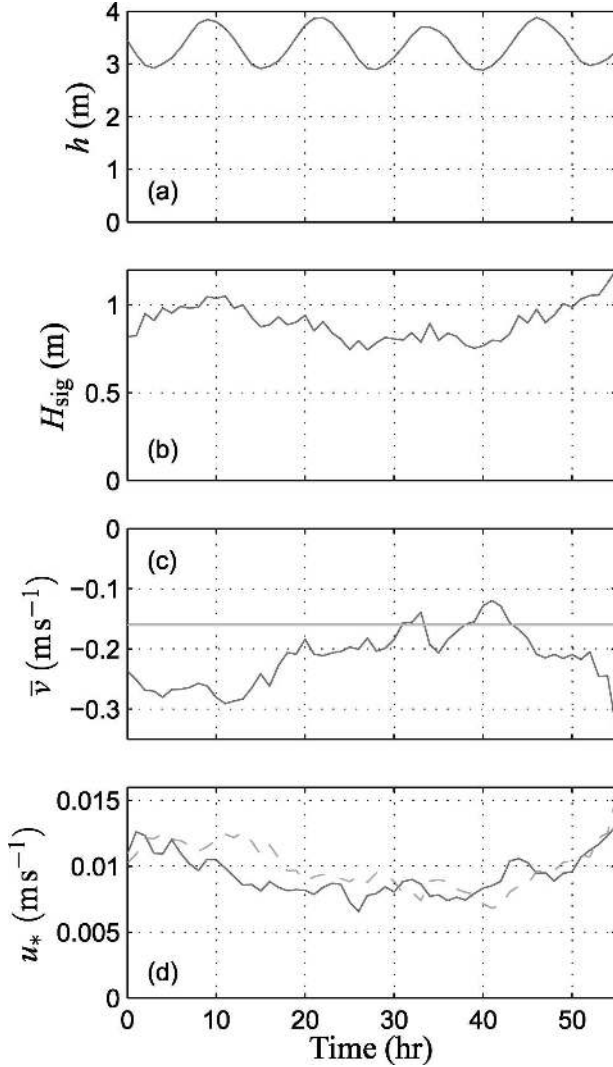Consistent with (2), friction velocities u_* calculated

FIG. 3. Time series of (a) depth h, (b) significant wave height H_{sig}, (c) alongshore current $\bar{v}$ at ADV 1, and (d) friction velocity u_*. The horizontal gray line in (c) indicates the $\bar{v} < -0.16$ m s^{-1} cutoff for non-flow-disturbance conditions. In (d), both wind stress (solid) and bottom stress (dashed) inferred u_* are shown.

from the wind stress (i.e., $u_*^2 = |\boldsymbol{\tau}|/\rho$) and from the parameterized bottom stress (i.e., $u_*^2 = c_d\overline{|\mathbf{u}|^2}$) are similar (Fig. 3d), varying between (5 and 15) $\times 10^{-3}$ m s^{-1}. For the analysis in section 4, the bottom stress–derived u_* (dashed line in Fig. 3d) is used. There is no significant difference in using either u_*.

3. Calculating dissipation

Dissipation ε is estimated by using the observed velocity (high) frequency spectrum together with the Lumley and Terray (1983) model for the effect of waves on the turbulent wavenumber spectrum (see appendix).

This method is similar to the semianalytic method used by Trowbridge and Elgar (2001); however, less-restrictive assumptions are used.

Velocity spectra [$S_{uu}(\omega)$, $S_{vv}(\omega)$, and $S_{ww}(\omega)$, where ω is the radian frequency] are calculated at each ADV over the entire burst (24.8 min) using 50-s-long segments (detrended, with Hamming window applied) with 50% overlapping, resulting in 120 degrees of freedom. At high frequencies (>3 Hz), the ADVs have an approximately constant noise floor that is lower for the component of flow parallel to the ADV orientation (i.e., at ADV 1 the S_{ww} noise floor is lower).

With the assumption of unidirectional wave-orbital motions ($\sigma_2 = \sigma_3 = 0$), Trowbridge and Elgar (2001) showed that in an inertial subrange at high frequencies (with no instrument noise)

$$(12/21)[S_{uu}(\omega) + S_{vv}(\omega)] = S_{ww}(\omega). \qquad (3)$$

The consistency of their ε was checked by examining the ratio R defined as

$$R = \frac{(12/21)\langle \omega^{5/3}[S_{uu}(\omega) + S_{vv}(\omega) - \text{noise}]\rangle}{\langle \omega^{5/3}S_{ww}(\omega)\rangle}, \qquad (4)$$

where $\langle\rangle$ represents an average over cyclic frequencies between 1 and 2 Hz, and noise is the constant u and v ADV noise floor. Trowbridge and Elgar (2001) observed that the numerator and denominator of R were highly correlated, with R near 1, indicating the presence of a turbulent inertial subrange. Estimating ε in this frequency range was thus deemed appropriate.

To test the appropriateness of estimating ε with these observations, the ratio R is calculated by averaging both the numerator and denominator over the cyclic frequencies 1.2–2 Hz at ADV 1 (only ADV 1 was upward looking). The noise floor was estimated as the average of $S_{uu} + S_{vv}$ over cyclic frequencies between 3 and 6 Hz. The numerator and denominator of R are highly correlated ($r = 0.97$) and the ratio R is typically between 1 and 1.5 with an average of 1.08 (Fig. 4). This also suggests that an inertial subrange of turbulence is observed and that dissipation can be estimated in this frequency range.

To minimize the effect of instrument noise, vertical velocities w' (parallel to the ADV body) in the ADV coordinate frame (as opposed to the rotated FRF coordinate frame) are used to calculate spectra. Only small differences occur between using the w' velocities and the w (ADV 1) or v (ADV 2 and 3) components. Dissipation $\varepsilon(\omega)$ is calculated at various radian frequencies (see appendix) with

$$\varepsilon(\omega) = \left[\frac{S_{w'w'}(\omega)2(2\pi)^{3/2}}{\alpha M_{w'w'}(\omega)}\right]^{3/2}, \qquad (5)$$
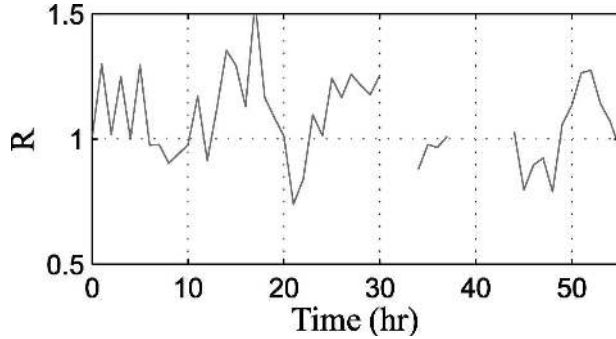
FIG. 4. Time series of ratio R [(4)] averaged over frequencies from 1.2 to 2 Hz during non-flow-disturbance times ($\bar{v} < -0.16$ m s^{-1}). The average of this R is 1.08.

where $\alpha = 1.5$ is Kolmogorov's constant, $S_{w'w'}(\omega)$ is the observed w' velocity spectrum, and $M_{w'w'}(\omega)$ is an integral over three-dimensional wavenumber space (Lumley and Terray 1983) that depends on the mean flow and the wave-orbital velocities (see appendix).

Dissipation $\varepsilon(\omega)$ calculated from (5) at cyclic frequencies (1.2, 1.4, 1.6, 1.8, and 2 Hz) are consistent with each other (Fig. 5), further indicating that the model for wave advection of frozen inertial-subrange turbulence (Lumley and Terray 1983) is reasonable. Because $\log[\varepsilon(\omega)]$ is closer to Gaussian distributed (in ω) than $\varepsilon(\omega)$, the frequency-averaged ε is calculated with a log mean; that is, $\varepsilon = \exp\{\langle\log[\varepsilon(\omega)]\rangle\}$, where $\langle\rangle$ represents an average over radian frequencies. However, there is no significant difference in the results using a standard average [i.e., $\varepsilon = \langle\varepsilon(\omega)\rangle$].

As a final check on the ε estimates, this integration method for calculating ε (see appendix) is compared with the method used by Trowbridge and Elgar (2001). For conditions where the Trowbridge and Elgar (2001) method is valid ($\sigma_2 = \sigma_3 = 0$) both the semianalytical (TE01) and present paper's integration (hereinafter FTW) method give the same results (see appendix). Trowbridge and Elgar (2001) applied their method to field data for which σ_2, $\sigma_3 \neq 0$. Nevertheless, their estimated ε was consistent with bottom boundary layer turbulence dynamics. The two ε estimation methods are compared at ADV 1 (the only upward-looking ADV). Both estimates are linearly related with a slope of one and high correlation (Fig. 6), giving further confidence that the dissipation estimates at the other ADVs are reasonable.

For the subsequent analysis, an EOF decomposition (Davis 1976) is performed on $\log[\varepsilon(z, t)]$ as opposed to $\varepsilon(z, t)$ because the time series of $\log[\varepsilon(z, t)]$ is more Gaussian distributed. An EOF (which compactly reproduces the greatest amount of variance) of $\varepsilon(z, t)$ will be
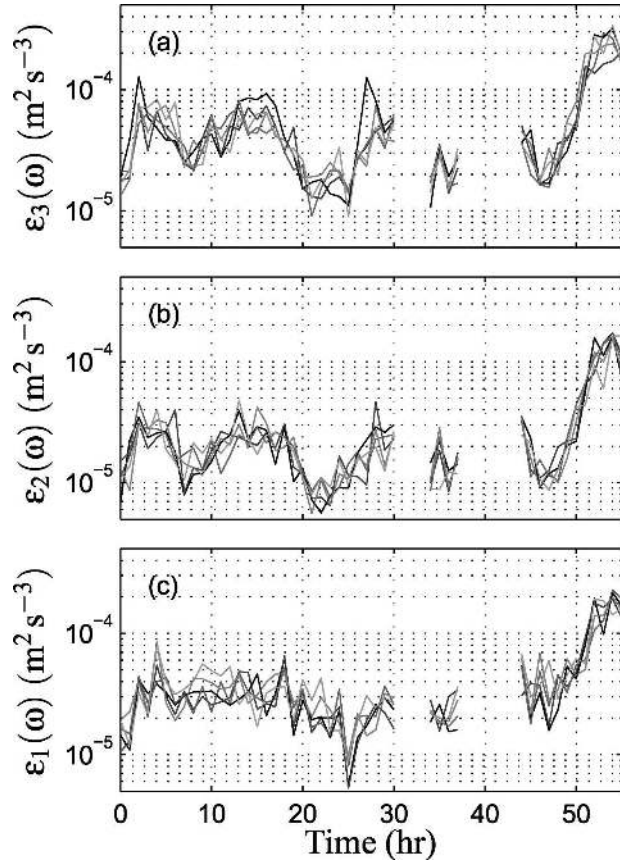

FIG. 5. Time series of $\varepsilon(\omega)$ at (a) ADV 3, (b) ADV 2, and (c) ADV 1. The ε is shown at cyclic frequencies 1.2, 1.4, 1.6, 1.8, and 2 Hz.

biased strongly toward the few largest dissipation events. The log-EOF decomposition is written as

$$\log[\varepsilon(z_j, t)] = M(z_j) + \sum_{i=1}^{3} a_i(t)E_i(z_j),$$

where z_j are the instrument heights, $M(z_j)$ is the mean, and E_i and a_i are the EOF and amplitudes, respectively. The first EOF reproduces 91% of the $\log(\varepsilon)$ variance. To remove noise from the ε signal a log-EOF1 dissipation $\tilde{\varepsilon}$ is constructed solely from the mean and first EOF,

$$\tilde{\varepsilon}(z_j, t) = \exp[M(z_j) + a_1(t)E_1(z_j)].$$

This log-EOF1 $\tilde{\varepsilon}$ is similar to the estimated ε at all ADV (Fig. 7) with log correlations ranging between $r = 0.91$ and 0.98.[1] For the remainder of the paper, the log-EOF1 $\tilde{\varepsilon}$ are used because of the reduction in

---

[1] Log correlation is the correlation between the log of the two quantities.
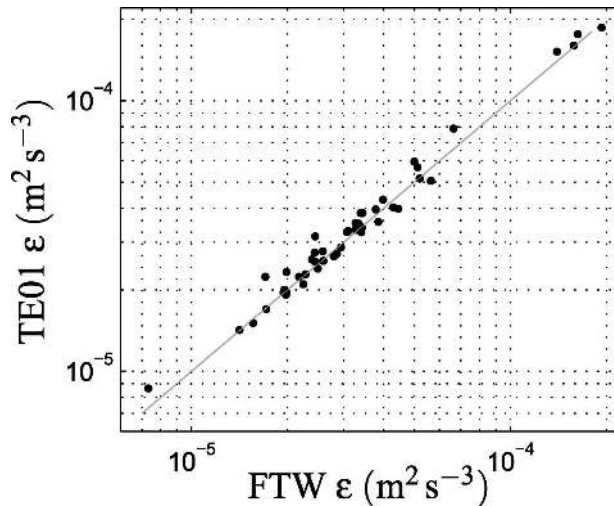
FIG. 6. ADV 1 dissipation ε_1 derived from the Trowbridge and Elgar (2001; TE01) method vs that derived with the method described here (FTW). The solid line is the 1:1 curve. The log correlation is high ($r = 0.99$) and the best-fit slope is indistinguishable from 1.

noise, although the tilde is dropped. The results do not change in any significant manner if the observed or log-EOF1 ε (e.g., dashed or solid lines in Fig. 7) are used. Hereinafter ε_1 (or ε_2, ε_3) denotes dissipation at ADV 1 (or 2, 3).

4. Results

a. Vertical structure of dissipation

The EOF decomposition provides information about the typical vertical structure of ε (Fig. 8). The vertical structure is derived from the mean and first EOF {e.g., $\exp[M(z_j) \pm \lambda_1 E_1(z_j)]$, where λ_1^2 is the $a_1(t)$ variance}. At all three locations, ε varies between 10^{-5} and 10^{-4} $m^2 s^{-3}$, comparable to the ε observed in 4.5-m water depth at the same beach (Trowbridge and Elgar 2001). At the uppermost ADV 3 ($z = 1.86$ m), ε_3 is maximum indicating that the surface is the dominant turbulence source. At the middle ADV 2 ($z = 1.32$ m), ε_2 is minimum and a factor of 2–2.5 smaller than ε_1. At the lowest ADV 1 ($z = 0.56$ m), ε_1 has a secondary maximum that is a factor of 1.5–1.8 larger than ε_2. This two-maxima ε vertical structure differs from that under deep-water breaking waves (e.g., Terray et al. 1996) and in continental shelf bottom boundary layers (e.g., Shaw et al. 2001), but could be seen as a combination of the two. The ε_3 maximum could be due to whitecapping breaking-wave–generated turbulence. The ε_1 secondary maximum could be due to BBL-generated turbulence or some other process. The causes for this observed ε magnitude and vertical structure are explored further.
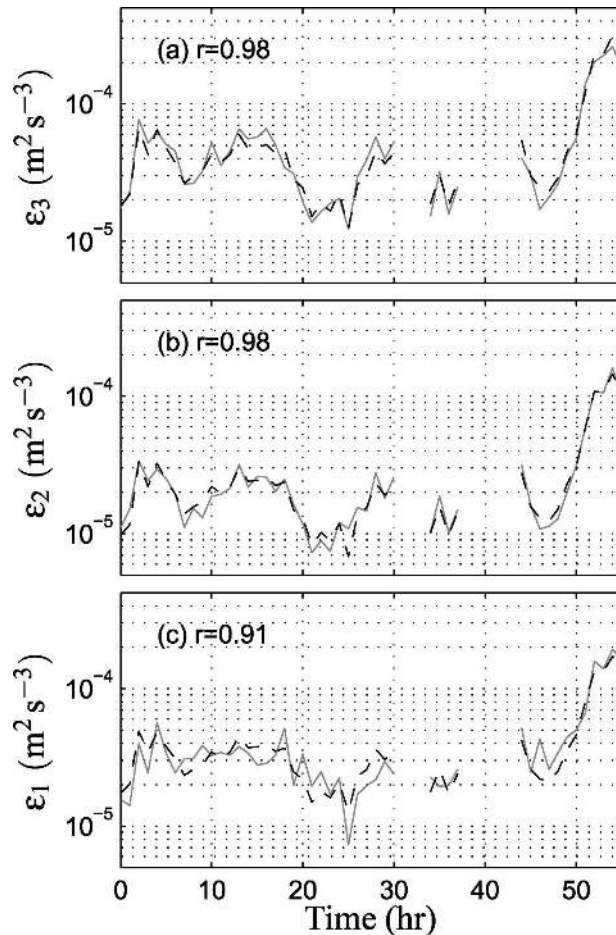

FIG. 7. Time series of observed ε (solid) and log-EOF1-derived $\tilde{\varepsilon}$ (dashed) at, from highest in the water column down, (a) ADV 3, (b) ADV 2, and (c) ADV 1. The correlations r between $\log(\varepsilon)$ and $\log(\tilde{N})$ are indicated in (a)–(c).

b. Surfzone scaling of dissipation

Although no depth-limited breaking was observed, the instrument tripod is in fairly shallow water (3.2 m on average). The ε_3 maximum suggests a surface source of turbulence, so a surfzone ε scaling (Feddersen and Trowbridge 2005) is examined as a possible explanation. Previously collected surfzone (with depth-limited wave breaking) ε datasets on different beaches (George et al. 1994; Bryan et al. 2003) were collapsed into a function of z/h when nondimensionalized as $\varepsilon/(g^3h)^{1/2}$ (Feddersen and Trowbridge 2005). When similarly nondimensionalized, these $\varepsilon/(g^3h)^{1/2}$ observations are much weaker (factor of 100) than surfzone observations (Fig. 9). This result highlights the differences between depth-limited breaking and the whitecapping breaking observed here as a turbulence source. The surfzone (50–100 m farther onshore) is a place of much stronger ε.
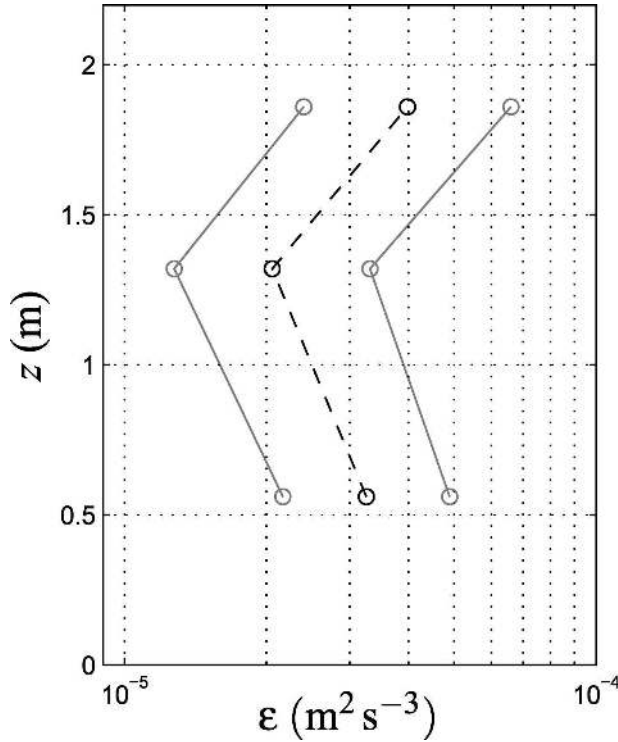
FIG. 8. EOF1-derived ε vertical structure mean (dashed) and $\pm$ standard deviation (solid).

c. Bottom and surface boundary layer scaling

Classic bottom (Grant and Madsen 1979) and wind-driven surface (Csanady 1984) boundary layer scalings for dissipation ε are [e.g., (1)]

$$\varepsilon = \frac{u_*^3}{\kappa z} \quad \text{and} \tag{6a}$$

$$\varepsilon = \frac{u_*^3}{\kappa z'}, \tag{6b}$$

respectively, where κ is von Kármán's constant, z is the height above the bed, and z' is the distance below the mean surface ($z' = h - z$). These scalings assume that the boundary layer dynamics are shear production P (i.e., $P = u_*^2 d\bar{v}/dz$) balancing ε, and do not include the effects of breaking-wave-generated turbulence. These boundary layer scalings are tested with the data.

The observed ε are larger than (factor of 8, 12, and 32 at ADVs 1, 2, and 3, respectively) the bottom boundary layer scaling (Fig. 10a), although the two are correlated ($r = 0.61$). At ADV 1, the ratio $\varepsilon \kappa z / u_*^3$ is on average 8, thus an underestimation of the stress u_*^2 (and the drag coefficient c_d) by a factor of 4 is required to make the bottom boundary layer scaling plausible. The observed
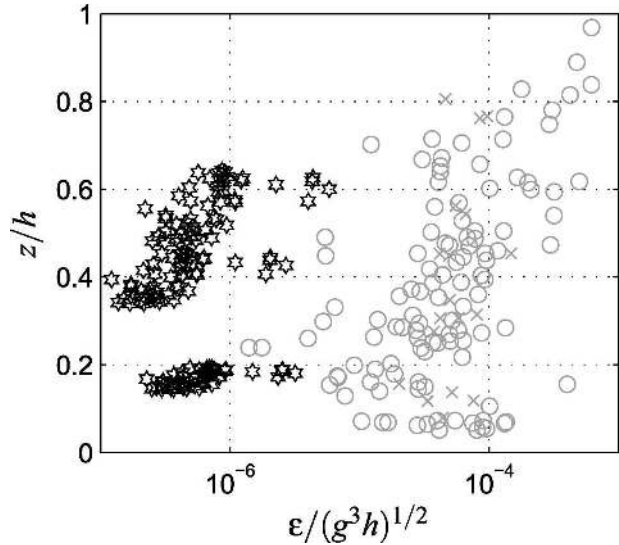

FIG. 9. Surfzone-scaled dissipation $\varepsilon/(g^3 h)^{1/2}$ as a function of normalized depth z/h. The stars represent the observations reported here. The circles and crosses represent the observations of George et al. (1994) and Bryan et al. (2003), respectively.

ε are also larger than (factor of 36, 17, and 24 at ADVs 1, 2, and 3, respectively) but correlated with ($r \approx 0.68$–0.70) the surface boundary layer scaling $u_*^3/(\kappa z')$ (Fig. 10b). This increased ε relative to surface layer scaling resembles deep-water observations (e.g., Agrawal et al. 1992). Thus although the correlations are high, it appears unlikely that these boundary layer scalings that neglect breaking-wave-generated turbulence are applicable.

d. Deep-water wave-breaking (Terray et al. 1996) scaling

In deep water, wave-breaking conditions (Terray et al. 1996) showed that near-surface dissipation scaled as

$$\frac{\varepsilon H_{\text{sig}}}{F} = 0.3 \left(\frac{z'}{H_{\text{sig}}} \right)^{-2}, \tag{7}$$

where F is the breaking-wave-induced flux of turbulent kinetic energy (TKE) into the water column, which Terray et al. (1996) parameterized as $F = \bar{c} u_*^2$, where $\bar{c}$ is an "effective phase speed." Here the Craig and Banner (1994) formulation $F = \alpha u_*^3$ is used, thus $\alpha = \bar{c}/u_*$. Model studies with $\alpha = 100$ reproduced this scaling (7) (e.g., Burchard 2001). In general, α depends on wave age c_p/u_* (where c_p is the wave phase speed). The α value appropriate for the nearshore is unknown.

The nearshore ε observations are scaled with (7) but with the (z'/H_{sig}) exponent and α estimated by linear regression. The scaled ε_2 and ε_3 follow (7) with best-fit values $\alpha = 250$ and exponent -1.9, close to the -2
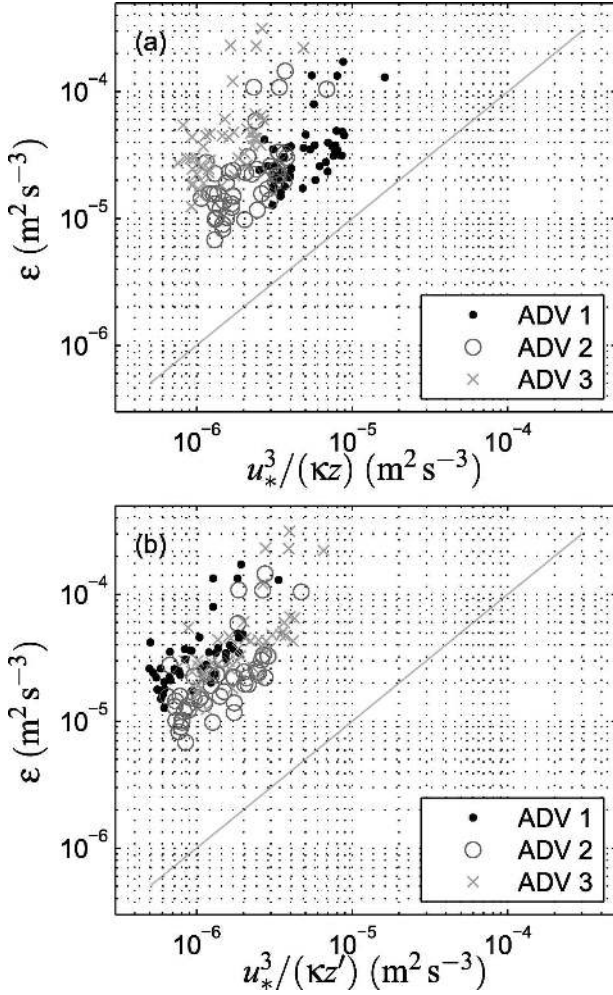
FIG. 10. Observed ε vs (a) bottom boundary layer scaling $u_*^3/(\kappa z)$ and (b) surface boundary layer scaling $u_*^3/(\kappa z')$ at ADVs 1 (dots), 2 (circles), and 3 (crosses).

FIG. 11. (a) Wave-scaled $\varepsilon H_{sig}/(\alpha u_*^3)$ vs wave-normalized depth z'/H_{sig} and (b) log–log plot of the same at only ADVs 2 and 3 with correlation $|r| = 0.73$. The solid line is the Terray et al. (1996) scaling of $\varepsilon H_{sig}/(\alpha u_*^3) = 0.3(z'/H_{sig})^{-2}$ with best-fit $\alpha = 250$. The best-fit exponent is -1.9, close to the Terray et al. (1996) parameterization exponent of -2.

exponent in (7) (Fig. 11), with log correlation of $|r| = 0.73$ (Fig. 11b). This indicates that in the upper-to-middle part of the water column, the processes governing ε are essentially the same as in deep water. However, the best-fit $\alpha = 250$ is 2.5 times that used in deep-water model studies (Craig and Banner 1994; Burchard 2001), suggesting a different F dependence on u_* in shallow water. The near-bed ε_1 secondary maximum (e.g., Fig. 8) does not follow the Terray et al. (1996) scaling (Fig. 11a), which requires ε to decrease monotonically with z'. The best-fit value of α and the ε_1 secondary maximum will be discussed further in section 4.

e. Shear production and buoyancy flux

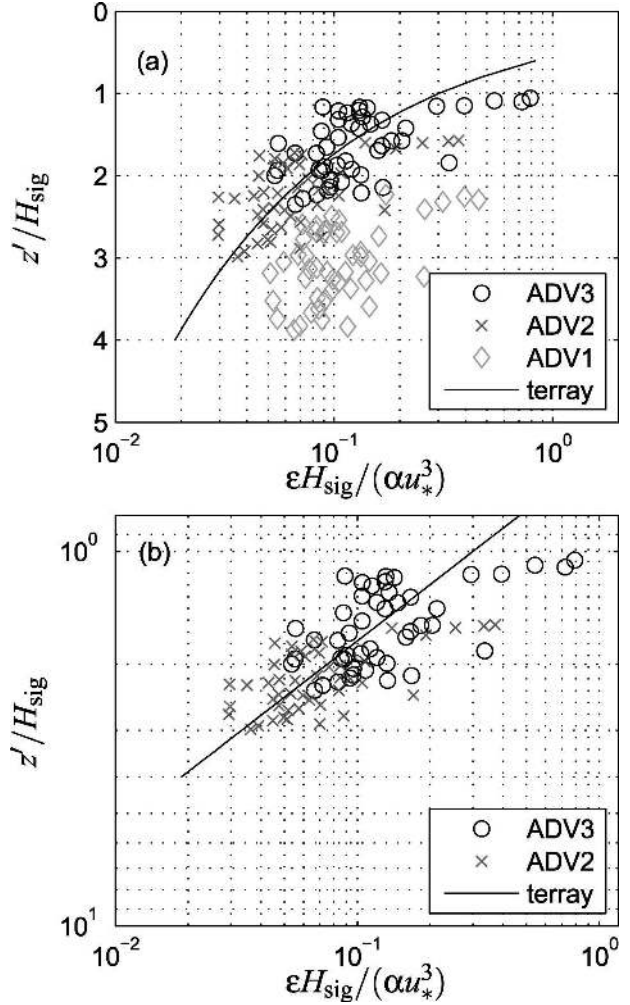The bottom boundary layer scaling (6a) is a factor of 8–10 too small to explain dissipation at ADV 1, but the

correlations are high, and it is possible that u_* is underestimated. This would require a factor of 4–4.5 underprediction of the stress u_*^2 and the bottom drag coefficient c_d. A seaward of the surfzone $c_d = 4 \times 10^{-3}$ is highly unlikely (Feddersen et al. 1998, 2004). Nevertheless, if bottom boundary layer scaling (6a) were applicable then bottom boundary layer turbulence dynamics would be expected to hold. These dynamics are a shear production P and dissipation balance $P = \varepsilon$, where

$$P = u_*^2 \frac{\partial \overline{v}}{\partial z} \qquad (8)$$

for a pure alongshore current. Trowbridge and Elgar (2001) found a $\varepsilon = P$ balance in 4.5-m mean water
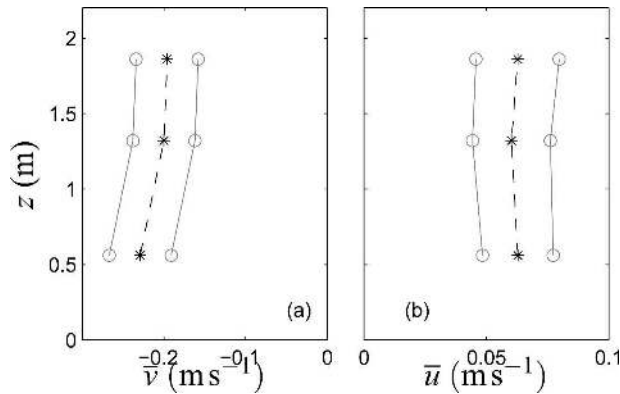
FIG. 12. EOF1-derived vertical profiles of current means (dashed) $\pm$ 1 standard deviation (solid): (a) $\bar{v}$ and (b) $\bar{u}$.

depth when there was wave breaking, strong $\bar{v}$, and strong $\partial \bar{v}/\partial z$.

To examine shear production, EOF decompositions are performed on the vertical structure of $\bar{v}$ and $\bar{u}$, respectively. The first EOF explains 99% and 93% of the variance of $\bar{v}$ and $\bar{u}$, respectively, and the mean and the first EOF are used to reconstruct $\bar{v}$ and $\bar{u}$ (Fig. 12). During non-flow-disturbance times, $|\bar{v}|$ is typically 0.15–0.25 m s^{-1}, and $\bar{u}$ is much weaker with offshore flow around 0.06 m s^{-1}. Curiously, $\bar{v}$ increases closer to the bed, and the vertical shear $\partial \bar{v}/\partial z$ has the opposite sign of $\bar{v}$ between both sets of ADVs (Fig. 12a). This is opposite of a typical boundary layer flow. Assuming the stress has the same sign as $\bar{v}$ (customary in quadratic drag), this implies energy transfer from turbulence to mean flow. ADV 1 sensor misalignment would map either $\bar{u}$ or $\bar{w}$ into $\bar{v}$, possibly explaining the increased $\bar{v}$. However, the mean $\bar{w}$ are consistently small ($<$1 cm s^{-1}), and the vertical and horizontal orbital velocity variances are consistent with linear theory. The inferred wave angles at all three ADVs are also consistent (rms angle differences $<1.5°$), ruling out rotation in the x–y plane. Thus sensor misalignment cannot explain the increased $\bar{v}$ at ADV 1. The EOF-reconstructed $\bar{u}$ does actually have shear $\partial u/\partial z$ of the same sign as $\bar{u}$ (Fig. 12b), but between ADVs 1 and 2, the $\bar{u}$ shear is a factor of 7–10 weaker than the $\bar{v}$ shear.

Although the sign of the shear implies negative production, the magnitude of the implied production $|P|$ [calculated using (8)] is weak relative to the ε (Fig. 13). Adding the $\bar{u}$ shear changes $|P|$ negligibly. The shear production between sensors 2 and 1 (P_{21}) is stronger than between sensors 3 and 2 (P_{32}), the result of the stronger $\partial \bar{v}/\partial z$ between sensors 1 and 2 (Fig. 12a). Shear production between ADVs 1 and 2 $|P_{21}|$ is on average a factor of 8 (6) smaller than ε_1 (ε_2) (Fig. 13a). Between ADVs 2 and 3, the shear production $|P_{32}|$ is much
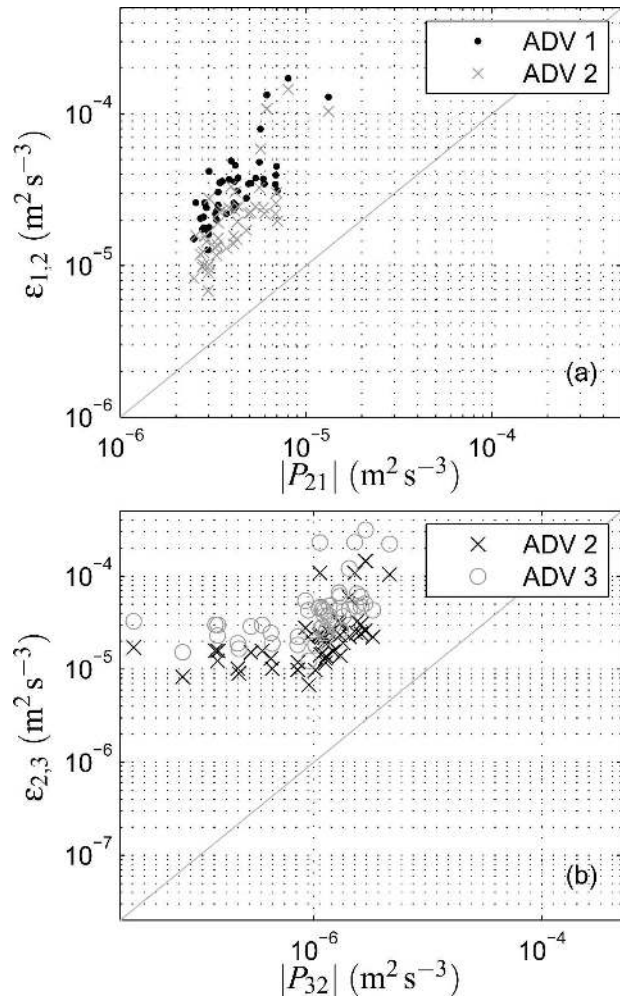
FIG. 13. Shear production magnitude $|P|$ vs ε at (a) ε_1 and ε_2 vs $|P_{21}|$ and (b) ε_2 and ε_3 vs $|P_{32}|$.

weaker than $|P_{21}|$, and is on average a factor of 40 (80) smaller than ε_2 (ε_3) (Fig. 13b). That $|P| \ll \varepsilon$ suggests that the vertical diffusion of TKE dominates over the entire water column. The ratio $h/H_{sig} \lesssim 5$ and in deepwater breaking-wave-generated turbulence penetrates at least this far (e.g., Terray et al. 1996; Burchard 2001), so this is consistent.

In stratified boundary layer flows, buoyancy flux B is also an important component to the dynamics. A vertical array of temperature sensors (sampling at 30 s) were deployed on the tripod. However, the vertical temperature variation was almost always within the measurement error (0.1°C). Thus there was likely no density gradient to support the buoyancy flux. Furthermore, in general turbulent stratified flows the flux Richardson number B/P is usually $<$0.2 (e.g., Gargett and Moum 1995; Moum 1996), suggesting that buoyancy flux cannot play a significant role.

5. Discussion

a. Nearshore Terray scaling

The best-fit $\alpha = 250$ in the parameterization of the surface TKE flux $F = \alpha u_*^3$ is a factor of 2.5 larger than that used in modeling ε under deep-water breaking waves (Craig and Banner 1994; Burchard 2001). This apparent difference between deep and shallow water is examined in greater detail.

Assuming a balance between wave growth and dissipation, Terray et al. (1996) developed a deep-water parameterization for $\alpha u_*/c_p$ (Terray et al. define $\bar{c} = \alpha u_*$) that depended on inverse wave age u_{*a}/c_p (u_{*a} is the air side friction velocity). For $u_* = 0.01$ m s^{-1} (Fig. 3d) and typical depths and wave periods, the inverse wave age $u_{*a}/c_p \approx 0.6$, yielding $\alpha u_*/c_p \approx 0.35$ (Terray et al. 1996, their Fig. 6) and $\alpha \approx 190$. This α is close (25% smaller) to the best-fit $\alpha = 250$ (Fig. 11) and is a factor of 2 larger than the $\alpha = 100$ used in deep-water modeling. Thus the best-fit α is largely consistent with the Terray et al. (1996) TKE flux parameterization. The 25% difference may be due to uncertainties in the data or may not be significant given the scatter in the Terray et al. (1996) data. However, in intermediate and shallow water, whitecapping wave breaking is more likely than in deep water given the same wind or wave conditions (Babanin et al. 2001), resulting in an increased breaking-wave-induced TKE flux for the same u_* and thus possibly a larger α.

b. Scaling the near-bed dissipation

The increased ε_1 cannot be explained as the result of turbulent shear flow (the shear production is too weak and ε_1 does not follow a BBL scaling), nor is it consistent with the Terray et al. (1996) scaling of ε decreasing monotonically away from the surface (7). An explanation for the increased dissipation at ADV 1 over ADV 2 (e.g., Fig. 8) is that the turbulent length scale l decreases closer to the bed, increasing ε through (e.g., Tennekes and Lumley 1972)

$$\varepsilon = (C_\mu)^3 \frac{k^{3/2}}{l}, \qquad (9)$$

where k is the turbulent kinetic energy and C_μ is a constant. This hypothesis is examined using the standard two-equation k–ε turbulence model (e.g., Reynolds 1976; Rodi 1987).

The k–ε equations for turbulent vertical diffusion balancing dissipation (the presumed dynamics under the breaking waves; Craig and Banner 1994; Burchard 2001) are
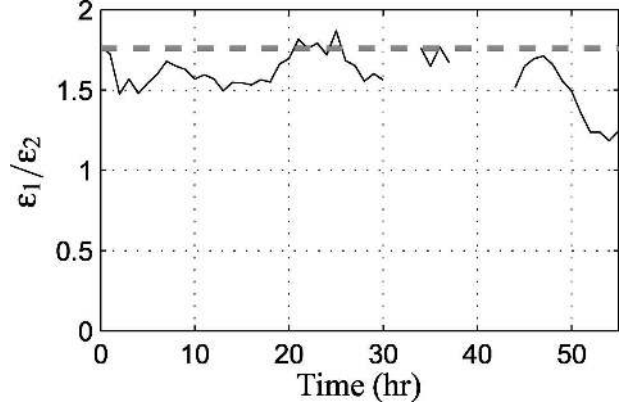

FIG. 14. Time series of the observed ratio $\varepsilon_1/\varepsilon_2$. The thick dashed line is the $k - \varepsilon$ based (12) ratio value of 1.75.

$$C_\mu \frac{\partial}{\partial z}\left(k^{1/2}l\frac{\partial k}{\partial z}\right) = C_\mu^3 \frac{k^{3/2}}{l} \quad \text{and}$$

$$(10a)$$

$$\frac{C_\mu}{\sigma_\varepsilon}\frac{\partial}{\partial z}\left[k^{1/2}l\frac{\partial(C_\mu^3 k^{3/2}/l)}{\partial z}\right] = C_{2\varepsilon}C_\mu^6 \frac{k^2}{l^2}, \qquad (10b)$$

where the vertical eddy viscosity for turbulence is given by $C_\mu k^{1/2}l$ and the eddy viscosity for ε is the same only modified by σ_ε^{-1}. Following Umlauf and Burchard (2003), the solutions for k and l can be written as $k = k_0 z^\beta$ and $l = l_0 z$ (where z is the near the bed) and substituted into (10), resulting in a quadratic relation for β (e.g., Umlauf and Burchard 2003),

$$(3\beta/2 - 1)(2\beta - 1) = (3/2)C_{2\varepsilon}\sigma_\varepsilon\beta^2, \qquad (11)$$

which depends only on $C_{2\varepsilon}$ and σ_ε. The standard k–ε value $C_{2\varepsilon} = 1.92$ (Reynolds 1976; Rodi 1987) is chosen. As discussed in Burchard (2001), σ_ε is a function of the ratio of shear production to dissipation (P/ε). In the limit of no shear production $\sigma_\varepsilon = 2.4$, which is used here. With these parameters and assuming a downward flux of turbulence, $k \sim z^{0.23}$, and the resulting dissipation $\varepsilon \sim k^{3/2}/l \sim z^{-0.65}$ increases toward the bed.

This scaling is assumed to apply between ADV 2 and ADV 1 and below (but above the wave boundary layer). This assumes that the vertical location of ADV 2 is the crossover point between the Terray et al. (1996) surface scaling and this near-bed scaling. With the near-bed scaling, the $\varepsilon_1/\varepsilon_2$ ratio becomes

$$\varepsilon_1/\varepsilon_2 = \left(\frac{z_1}{z_2}\right)^{-0.65} = \left(\frac{0.56}{1.32}\right)^{-0.65} = 1.75. \qquad (12)$$

The observed ratio $\varepsilon_1/\varepsilon_2$ mostly varies between 1.5 and 1.75 (Fig. 14) and is consistent with the ratio (12). Vary-

ing σ_ε within the range of boundary layer flow to shear-free turbulent decay (1.2–2.6) results in small changes (1.65–1.78) in the $\varepsilon_1/\varepsilon_2$ ratio. This indicates that the increased ε_1 is due to the length scale decreasing closer to the bed but with the same turbulence dynamics (turbulent diffusion balancing dissipation) as for deep-water wave breaking. It also suggests that the ADV 2 vertical location is near the crossover location between the Terray et al. (1996) and near-bed scaling.

c. Relation to other ε observations

Trowbridge and Elgar (2001) also observed nearshore ε, approximately 1 m above the bed in 4.5-m mean water depth. There were three significant ε events when P was also observed, all of which had large waves (with $H_{sig} > 1.5$ m). Two of these events had a $P = \varepsilon$ balance and strong alongshore currents ($\bar{v} > 0.5$ m s^{-1}). Modeling of the strongest event (yearday 292; Trowbridge and Elgar 2001, their Fig. 8) showed that at 1 m above the bed, bottom boundary layer–generated shear was the dominant process, but just higher in the water column, downward diffusion of breaking-wave-generated turbulence dominated (Feddersen and Trowbridge 2005). However, the other event (yearday 270) had strong dissipation $\varepsilon = 8 \times 10^{-5}$ m^2 s^{-3}, negligible P, and weak alongshore current ($|\bar{v}| < 0.05$ m s^{-1}). This is similar to what was observed here ($|P| \ll \varepsilon$).

The BBL scaling (6a) does not apply to these observations with weak alongshore currents ($|\bar{v}| < 0.3$ m s^{-1}), but the two $P = \varepsilon$ events in Trowbridge and Elgar (2001) suggest that at times it does, particularly with stronger alongshore currents. In quadratic bottom stress $u_* \sim \bar{v}$, and provided the whitecapping wave-breaking–generated turbulence source is constant, then a doubling (or tripling) of $\bar{v}$ would result in an eightfold (or 27-fold) increase ε. This suggests that with large $\bar{v}$, BBL dynamics would become important in the turbulence dynamics.

The estimated surface and bed friction velocities u_* are similar (Fig. 3d). However, in the nearshore, this is not always the case. The Terray et al. (1996) (7) and BBL (6a) scalings require as inputs the surface and bed friction velocities, respectively. The wide range of possible nearshore wave and current conditions results in different combinations of surface and bottom ε scalings. For example, with no waves and a pure alongshore wind, surface and bed u_* are the same and BL scaling (not breaking-wave scaling) is expected to apply. In contrast, with large waves, purely onshore-directed wind, and no currents, the surface and bed u_* will differ and the breaking-wave scaling would apply. Most nearshore conditions are between these two extremes.

6. Summary

Nearshore observations of turbulent dissipation ε at three vertical locations were made in 3.2-m water depth. The significant wave height was typically $H_{sig} < 1$ m, and this site was seaward of the surfzone with no depth-limited wave breaking. However, whitecapping-style wave breaking more typical of deep water did occur. At each location, ε was estimated from the observed velocity spectra and a kinematic turbulence model that includes the effects of waves. The observed velocity spectra are consistent with this model, and ε estimates at various frequencies are similar.

The first EOF of ε describes 91% of the $\log(\varepsilon)$ variance. The typical vertical structure of ε has a maximum closer to the surface and minimum at middepth, with a secondary maximum closer to the bed. The observed ε do not follow a surfzone scaling. Nor do they follow surface or bottom boundary layer scalings. However, for a stronger alongshore current, bottom boundary layer scalings may be applicable. At the uppermost two locations, the deep-water breaking-wave (Terray et al. 1996) scaling reproduces the top two ε. The dependence of the breaking-wave-induced TKE flux on the wind is consistent with the empirical results of Terray et al. (1996). This, in addition to the negligible observed shear production, indicates that downward diffusion of TKE is balancing ε. The near bed at ADV 1 ε does not follow this scaling. Instead of decreasing with depth, ε_1 increases, consistent with a decrease in the turbulent length scale near the bed. Thus, in the nearshore region seaward of the surfzone, whitecapping breaking-wave-generated turbulence can be significant and may dominate over boundary layer processes.

APPENDIX

Kinematic Turbulence Model for Estimating Dissipation

The Lumley and Terray (1983) model for how a random wave field affects the inertial-range turbulence wavenumber spectra is used to estimate ε. In the limit of frequencies much larger than the surface gravity wave peak frequency, the model for the measured tur-

bulence spectrum becomes [Lumley and Terray's (1983) Eq. (A11) and Trowbridge and Elgar's (2001) Eq. (A1)]

$$S_{lm}(\omega) = \frac{1}{2\pi} \int_{\mathbf{k}} \phi_{lm}(\mathbf{k}) \int_{-\infty}^{\infty} \exp\left[-\frac{1}{2}k_i k_j C_{ij} \tau^2\right.$$

$$\left. + i(k_i \bar{u}_i - \omega)\tau\right] d\tau \, d\mathbf{k}, \tag{A1}$$

where ω is the radian frequency, $S_{lm}(\omega)$ is the measured velocity spectrum defined so that $\int_{-\infty}^{\infty} S_{lm}(\omega)d\omega = \overline{u_l u_m}$, τ is a dummy integration variable, ϕ_{lm} is the wavenumber spectrum tensor of turbulence (Batchelor 1967), $\mathbf{k}$ is the wavenumber vector, and k_i is the wavenumber vector component. The orbital wave velocity covariance is given by C_{ij}, and $\bar{u}_i$ is the ith component of mean velocity. With indicial notation, the coordinate system is defined so that x_3 is the vertical (z), and x_1 is in the direction of the waves (i.e., principal axes of C_{ij}) so that for linear surface gravity waves C_{ij} is diagonal. By integrating over τ and completing the square, (A1) becomes

$$S_{lm}(\omega) = \frac{1}{\sqrt{2\pi}} \int_{\mathbf{k}} \frac{\phi_{lm}(\mathbf{k})}{\sqrt{k_i k_j C_{ij}}} \exp\left[-\frac{(k_i \bar{u}_i - \omega)^2}{2 k_i k_j C_{ij}}\right] d\mathbf{k}. \tag{A2}$$

The turbulence is assumed nearly homogeneous and isotropic with a Kolmogorov spectrum (Batchelor 1967)

$$E(k) = \alpha \varepsilon^{2/3} k^{-5/3},$$

where $k = |\mathbf{k}|$ and $\alpha = 1.5$ is the empirical Kolmogorov constant, so that

$$\phi_{lm}(\mathbf{k}) = \frac{E(k)}{4\pi k^2}\left(\delta_{lm} - \frac{k_l k_m}{k^2}\right)$$

$$= \frac{\alpha \varepsilon^{2/3}}{4\pi} k^{-11/3}\left(\delta_{lm} - \frac{k_l k_m}{k^2}\right). \tag{A3}$$

Substituting ϕ_{lm} into (A2) results in

$$S_{lm}(\omega) = \frac{\alpha \varepsilon^{2/3}}{2(2\pi)^{3/2}} M_{lm}(\omega), \tag{A4}$$

where $M_{lm}(\omega)$ is (with mean vertical velocity $\bar{u}_3 = 0$)

$$M_{lm}(\omega) = \int_{-\infty}^{\infty} \int_{-\infty}^{\infty} \int_{-\infty}^{\infty} \frac{k^{-11/3}\left(\delta_{lm} - \frac{k_l k_m}{k^2}\right)}{\sqrt{\sigma_i^2 k_i^2}}$$

$$\times \exp\left[-\frac{(k_1 \bar{u}_1 + k_2 \bar{u}_2 - \omega)^2}{2\sigma_i^2 k_i^2}\right] dk_1 \, dk_2 \, dk_3, \tag{A5}$$

analogous to Trowbridge and Elgar's (2001) (A4). The value of $M_{lm}(\omega)$, which depends solely on the mean currents and waves, is required in order to estimate ε from the observed spectra $S_{lm}(\omega)$. Departing from Trowbridge and Elgar (2001), the assumption that $\sigma_2 = \sigma_3 = 0$ is not made, and the integral (A5) is evaluated numerically using the observed $\bar{u}_i$ and σ_i.

Two coordinate transformations are applied to the integral (A5). The first is $\tilde{k}_i = \sigma_i k_i$, and the second transformation is spherical coordinates; that is,

$$\tilde{k}_1 = \rho \cos\phi \cos\theta, \quad \tilde{k}_2 = \rho \cos\phi \sin\theta, \quad \text{and} \quad \tilde{k}_3 = \rho \sin\phi,$$

resulting in

$$\sigma_i^2 k_i^2 = \rho^2, \quad d\mathbf{k} = \frac{\rho^2 \cos\phi}{\sigma_1 \sigma_2 \sigma_3} d\rho d\phi d\theta, \quad \text{and}$$

$$k^2 = \rho^2\left[\cos^2\phi\left(\frac{\cos^2\theta}{\sigma_1^2} + \frac{\sin^2\theta}{\sigma_2^2}\right) + \frac{\sin^2\phi}{\sigma_3^2}\right] = \gamma^2 \rho^2,$$

where γ is only a function of θ and ϕ. Note also that $[\delta_{lm} - (k_l k_m)/k^2]$ is only a function of θ and ϕ. With this the integral (A5) becomes

$$M_{lm}(\omega) = \int_0^{\infty} d\rho \, \rho^{-8/3} \int_{-\pi/2}^{\pi/2} \int_{-\pi}^{\pi} \gamma^{-11/3}\left(\delta_{lm} - \frac{k_l k_m}{k^2}\right) \exp\left\{\frac{-\left[\rho \cos\phi\left(\frac{\cos\theta \bar{u}_1}{\sigma_1} + \frac{\sin\theta \bar{u}_2}{\sigma_2}\right) - \omega\right]^2}{2\rho^2}\right\} \frac{\cos\phi \, d\theta \, d\phi}{\sigma_1 \sigma_2 \sigma_3}. \tag{A6}$$

It is straightforward to demonstrate that, for large ω,

$$M_{lm}(\omega) \sim \int_0^{\infty} d\rho \, \rho^{-8/3} \exp\left(\frac{-\omega^2}{2\rho^2}\right) \sim \omega^{-5/3}. \tag{A7}$$

The integral (A6) is numerically integrated with finite

differences in θ and ϕ coordinates, and with logarithmically transformed finite differences in ρ coordinates. At large ρ a tail based on (A7) is patched onto the integral, typically adding less than 0.01% to the integral.

a. Tests

The numerical integral method reproduces the analytic result for a pure current case. A more significant test of the method is a comparison with the Trowbridge and Elgar (2001) method. For $\sigma_2 = \sigma_3 = \bar{u}_1 = 0$,

Trowbridge and Elgar (2001) showed that $M_{33} = (4/7) \times (M_{11} + M_{22})$ and

$$M_{33}(\omega) = \frac{12}{55} 2(2\pi)^{3/2} \bar{u}_2^{2/3} \omega^{-5/3} I(\sigma_1/\bar{u}_2, \pi/2),$$

with

$$I(\sigma_1/\bar{u}_2, \theta) = \frac{1}{\sqrt{2\pi}} \left(\frac{\sigma_1}{\bar{u}_2} \right)^{2/3} \int_{-\infty}^{\infty} \left[x^2 - 2\frac{\bar{u}_2}{\sigma_1} \cos(\theta) x + \frac{\bar{u}_2^2}{\sigma_1^2} \right]^{1/3} \exp\left(-\frac{1}{2} x^2 \right) dx. \tag{A8}$$

The numerical integration method (A5) with $\sigma_2 = \sigma_3 = 0.01$ m s^{-1} is compared with the Trowbridge and Elgar (2001) method. The numerical integrated (A5) M_{ij} reproduces $M_{33}(\omega) \sim \omega^{-5/3}$, $M_{33}(\omega) = (4/7)[M_{11}(\omega) + M_{22}(\omega)]$, and the Trowbridge and Elgar (2001) estimated ε to within 0.5% or better.

b. Testing the Trowbridge and Elgar (2001) method

The Trowbridge and Elgar (2001) method assumes that $\sigma_2 = \sigma_3 = 0$, which is not the case either in the nearshore or deep water. For example, in the conditions encountered here, σ_2 and σ_3 were typically one-half of σ_1, which may lead to errors in estimating ε using the Trowbridge and Elgar (2001) method. The accuracy of the Trowbridge and Elgar (2001) method is examined for typical conditions with $\sigma_2 = \sigma_3 = \sigma_1/2$ at frequency $f = 1.5$ Hz. For the conditions where $\bar{u}_2$ varies between 0.1 and 1.2 m s^{-1} and σ_u varies between 0.1 and 1.5 m s^{-1}, the ratio of ε derived from the 2 methods ($\varepsilon_{\text{FTW}}/\varepsilon_{\text{TE01}}$) is between 1 and 0.7 (Fig. A1). Similar

results are evident if $\sigma_3 = \sigma_1$ or at other frequencies and explain the similarity in the observed ε derived from the two methods (Fig. 6).

REFERENCES

Agrawal, Y. C., E. A. Terray, M. A. Donelan, P. A. Hwang, A. J. Williams, W. Drennan, K. Kahm, and S. Kitaigorodskii, 1992: Enhanced dissipation of kinetic energy beneath breaking waves. *Nature,* **359,** 219–220.

Anis, A., and J. N. Moum, 1995: Surface wave–turbulence interactions: Scaling $\varepsilon(z)$ near the sea surface. *J. Phys. Oceanogr.,* **25,** 2025–2045.

Babanin, A. V., I. R. Young, and M. L. Banner, 2001: Breaking probabilities for dominant surface waves on water of finite constant depth. *J. Geophys. Res.,* **106,** 11 659–11 676.

Batchelor, G. K., 1967: *The Theory of Homogeneous Turbulence.* Cambridge University Press, 197 pp.

Bryan, K. R., K. P. Black, and R. M. Gorman, 2003: Spectral estimates of dissipation rate within and near the surf zone. *J. Phys. Oceanogr.,* **33,** 979–993.

Burchard, H., 2001: Simulating the wave-enhanced layer under breaking surface waves with two-equation turbulence models. *J. Phys. Oceanogr.,* **31,** 3133–3145.

Craig, P. D., and M. L. Banner, 1994: Modeling wave-enhanced turbulence in the ocean surface layer. *J. Phys. Oceanogr.,* **24,** 2546–2559.

Csanady, G. T., 1984: The free surface turbulent shear layer. *J. Phys. Oceanogr.,* **14,** 402–411.

Davis, R. E., 1976: Predictability of sea surface temperature and sea level pressure anomalies over the North Pacific Ocean. *J. Phys. Oceanogr.,* **6,** 249–266.

Dewey, R. K., and W. R. Crawford, 1988: Bottom stress estimates from vertical dissipation rate profiles on the continental shelf. *J. Phys. Oceanogr.,* **18,** 1167–1177.

Donelan, M. A., 1990: Air–sea interaction. *The Sea,* B. LéMehauté and D. M. Hanes, Eds., Ocean Engineering Science, Vol. 9, John Wiley and Sons, 239–292.

Drennan, W. M., M. A. Donelan, E. A. Terray, and K. B. Katsaros, 1996: Oceanic turbulence dissipation measurements in SWADE. *J. Phys. Oceanogr.,* **26,** 808–815.

——, H. C. Graber, and M. A. Donelan, 1999: Evidence for the effects of swell and unsteady winds on marine wind stress. *J. Phys. Oceanogr.,* **29,** 1853–1864.
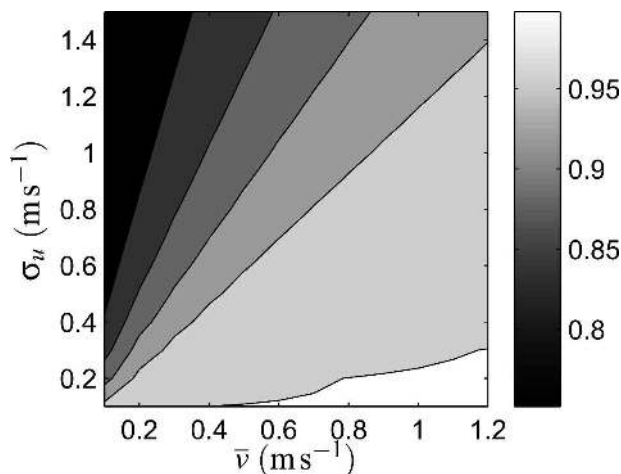
FIG. A1. Contour plot of $\varepsilon_{\text{FTW}}/\varepsilon_{\text{TE01}}$ (grayscale) as a function of $\bar{v}$ and σ_u for $\sigma_v = \sigma_w = \sigma_u/2$.

Elgar, S., R. T. Guza, and B. Raubenheimer, 2001: Current meter performance in the surfzone. *J. Atmos. Oceanic Technol.,* **18,** 1735–1746.

Feddersen, F., and J. H. Trowbridge, 2005: The effect of wave breaking on surfzone turbulence and alongshore currents: A modeling study. *J. Phys. Oceanogr.,* **35,** 2187–2203.

——, and A. J. Williams III, 2007: Direct estimation of the Reynolds stress vertical structure in the nearshore. *J. Atmos. Oceanic Technol.,* **24,** 102–116.

——, R. T. Guza, S. Elgar, and T. H. C. Herbers, 1998: Alongshore momentum balances in the nearshore. *J. Geophys. Res.,* **103,** 15 667–15 676.

——, ——, and ——, 2004: Inverse modeling of one-dimensional setup and alongshore current in the nearshore. *J. Phys. Oceanogr.,* **34,** 920–933.

Gargett, A. E., and J. N. Moum, 1995: Mixing efficiencies in turbulent tidal fronts: Results from direct and indirect measurement of density flux. *J. Phys. Oceanogr.,* **25,** 2583–2608.

George, R., R. E. Flick, and R. T. Guza, 1994: Observations of turbulence in the surf zone. *J. Geophys. Res.,* **99,** 801–810.

Grant, W. D., and O. S. Madsen, 1979: Combined wave and current interaction with a rough bottom. *J. Geophys. Res.,* **84,** 1797–1808.

Gross, T. F., and A. R. M. Nowell, 1985: Spectral scaling in a tidal boundary layer. *J. Phys. Oceanogr.,* **15,** 496–508.

Large, W. G., and S. Pond, 1981: Open ocean momentum flux measurements in moderate to strong winds. *J. Phys. Oceanogr.,* **11,** 324–336.

Lumley, J. L., and E. A. Terray, 1983: Kinematics of turbulence convected by a random wave field. *J. Phys. Oceanogr.,* **13,** 2000–2007.

Mellor, G. L., and T. Yamada, 1982: Development of a turbulence closure model for geophysical fluid problems. *Rev. Geophys.,* **20,** 851–875.

Moum, J. N., 1996: Efficiency of mixing in the main thermocline. *J. Geophys. Res.,* **101,** 12 059–12 069.

Peters, H., and R. Bokhorst, 2000: Microstructure observations of turbulent mixing in a partially mixed estuary. Part I: Dissipation rate. *J. Phys. Oceanogr.,* **30,** 1232–1244.

Reynolds, W. C., 1976: Computation of turbulent flow. *Annu. Rev. Fluid Mech.,* **8,** 183–207.

Rieder, K. F., J. A. Smith, and R. A. Weller, 1996: Some evidence of colinear wind stress and wave breaking. *J. Phys. Oceanogr.,* **26,** 2519–2524.

Rodi, W., 1987: Examples of calculation methods for flow and mixing in stratified fluid. *J. Geophys. Res.,* **92,** 5305–5328.

Shaw, W. J., J. H. Trowbridge, and A. J. Williams III, 2001: The budgets of turbulent kinetic energy and scalar variance in the continental shelf bottom boundary layer. *J. Geophys. Res.,* **106,** 9551–9564.

Soloviev, A., and R. Lukas, 2003: Observation of wave-enhanced turbulence in the near-surface layer of the ocean during TOGA COARE. *Deep-Sea Res. I,* **50,** 371–395.

Stips, A., H. Burchard, K. Bolding, H. Prandke, A. Simon, and A. Wüest, 2005: Measurement and simulation of viscous dissipation in the wave affected surface layer. *Deep-Sea Res. II,* **52,** 1133–1155.

Tennekes, H., and J. L. Lumley, 1972: *A First Course in Turbulence.* MIT Press, 300 pp.

Terray, E. A., M. A. Donelan, Y. C. Agrawal, W. M. Drennan, K. K. Kahma, A. J. Williams, and P. Hwang, 1996: Estimates of kinetic energy dissipation under breaking waves. *J. Phys. Oceanogr.,* **26,** 792–807.

——, W. M. Drennan, and M. A. Donelan, 1999: The vertical structure of shear and dissipation in the ocean surface layer. *Proc. Symp. on the Wind-Driven Air–Sea Interface-Electromagnetic and Acoustic Sensing, Wave Dynamics and Turbulent Fluxes,* Sydney, Australia, University of New South Wales, 239–245.

Trowbridge, J. H., and S. Elgar, 2001: Turbulence measurements in the surfzone. *J. Phys. Oceanogr.,* **31,** 2403–2417.

——, and ——, 2003: Spatial scales of stress-carrying nearshore turbulence. *J. Phys. Oceanogr.,* **33,** 1122–1128.

——, W. R. Geyer, M. M. Bowen, and A. J. Williams, 1999: Nearbottom turbulence measurements in a partially mixed estuary: Turbulent energy balance, velocity structure, and alongchannel momentum balance. *J. Phys. Oceanogr.,* **29,** 3056–3072.

Umlauf, L., and H. Burchard, 2003: A generic length-scale equation for geophysical turbulence models. *J. Mar. Res.,* **61,** 235–265.